

Accessing the Optical Magnetic Near-Field through Babinet's Principle

Honghua U. Yang,[†] Robert L. Olmon,[†] Kseniya S. Deryckx,[‡] Xiaoji G. Xu,^{†,§} Hans A. Bechtel,^{||} Yuancheng Xu,[⊥] Brian A. Lail,[⊥] and Markus B. Raschke^{*,†}

[†]Department of Physics, Department of Chemistry, and JILA, University of Colorado, Boulder, Colorado 80309, United States,

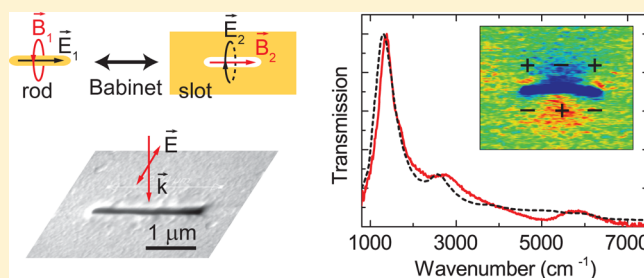
[‡]School of Medicine, University of Washington, Seattle, Washington 98195, United States,

^{||}Advanced Light Source Division, Lawrence Berkeley National Laboratory, 1 Cyclotron Road, Berkeley, California 94720, United States

[⊥]Department of Electrical and Computer Engineering, Florida Institute of Technology, Melbourne, Florida 32901, United States

ABSTRACT: Engineering the optical magnetic field with optical antennas or metamaterials extends the ways to control light-matter interaction. The slot antenna, as the electromagnetic dual of the linear rod antenna, provides the simplest form of a magnetic resonator tunable through its length. Using combined far- and near-field spectroscopy and imaging, and theory, we identify magnetic dipole and higher order bright and dark magnetic resonances at mid-infrared frequencies. From resonant length scaling and spatial near-field distribution, we confirm the applicability of Babinet's principle over the mid-infrared spectral region. Babinet's principle thus provides access to spatial and spectral magnetic field properties, leading to the targeted design of magnetic optical antennas.

KEYWORDS: optical magnetic field, IR antenna, slot antenna, Babinet's principle, near-field, duality



Controlling the optical magnetic field with optical antennas or metamaterials provides for new ways of tuning the near-field light-matter interaction.¹⁻⁵ Because the magnetic dipole transition probability is in general $\sim 10^4$ times smaller than the electric dipole transition, the magnetic response at optical frequencies is typically weak.⁶⁻⁸ However, in addition to the transition moment, the interaction rate highly depends on the electromagnetic local density of states (EM-LDOS), which can be modified through the local environment. Examples include the use of magnetic plasmonic structures for magnetic field enhancement over 100 times,⁹⁻¹¹ achieving magnetic nonlinear effects with metamaterials,¹² nanorod metamaterials for biosensing,¹³ or tailoring the magnetic dipole emission with plasmonic structures.¹⁴

Despite the prominent role of the magnetic field in many nano-optical devices, probing magnetic resonances and local magnetic near-field properties, as desirable for design and device performance evaluation, has remained difficult.¹⁵⁻¹⁸ Vector-resolved electric near-field measurements at optical frequencies using scanning near-field probes can be used to derive the magnetic field through Maxwell's equations.^{16,19} Equally indirect, aperture-based near-field imaging allows one to investigate the magnetic field coupled through a fiber.^{15,20-22} However, these methods require specially fabricated nanoprobe or numerical modeling for data interpretation.

Here we demonstrate experimentally and theoretically the application of Babinet's principle in the infrared (IR) as a

generalized principle to gain insight into the spatio-spectral properties of magnetic resonances, specifically from the comparison of the optical rod and slot antenna as a prototypical system.²³⁻²⁹ We show that electromagnetic duality can be used to access the optical magnetic field and its structural resonance of optical rod antennas as the dual to the slot antenna in both its far-field spectral and near-field spatial response. This confirms that the theoretical requirement of Babinet's principle for the structure to be infinitely thin and perfectly conducting is still fulfilled to a good approximation in the IR.

As illustrated in Figure 1a, Babinet's principle provides a theoretical link between the electric and magnetic field of an electromagnetic structure and its complement.³⁰⁻³³ The fields of structure 1 (rod) and its complement 2 (slot), are related by $E_1/c = B_2$ and $E_2/c = -B_1$. Application of this principle provides spectroscopic and spatial access to the optical magnetic field of a structure by measuring the corresponding electric field properties of its complement. This approach is widely used in radio frequency (RF) antenna and THz metamaterial design,^{32,34,35} which we extend to the mid-IR.^{36,37} We also discuss the general range of validity of Babinet's principle throughout the entire electromagnetic spectrum.

Slot antennas were fabricated by focused ion beam (FIB) milling into a thermally evaporated 50 nm thick Au film on KBr

Received: June 12, 2014

Published: August 6, 2014

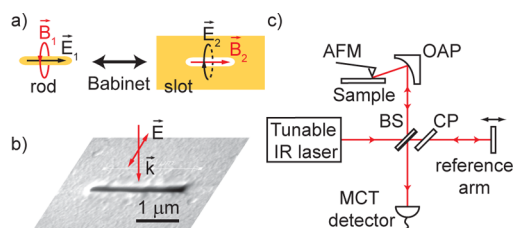


Figure 1. Babinet's principle (a). The electromagnetic field of a slot antenna and its complement linear rod antenna are related through Babinet's principle. (b) Scanning electron microscopy (SEM) image of a slot antenna, with an illustration of the incident laser field polarized perpendicular to the slot direction. (c) Scattering-type scanning near-field microscopy (s-SNOM), using tunable femtosecond OPO/DFG excitation and interferometric near-field detection.

and on silicon (with an approximately 3 nm native SiO₂ layer). The slot lengths range from 500 to 2600 nm with width of 150 nm. The individual slots are separated by >20 μm to allow for their individual far-field spectroscopic characterization. The Au thickness of 50 nm was chosen to be greater than the optical skin depth of Au of about 20 nm throughout the IR.³⁸

To determine the resonant wavelength of slot antennas, the transmission spectra of the individual slot antennas on a KBr substrate were measured using an IR microscope at Beamline 1.4 at the Advanced Light Source (ALS) synchrotron at Lawrence Berkeley National Laboratory, providing bandwidth from 800–10000 cm⁻¹. For illumination and collection two Schwarzschild type objectives were used (32 ×, NA = 0.65), with nominal incidence angle between 18° and 40° at focus. Spectra were measured using a Fourier transform infrared (FTIR) spectrometer (Nexus 870, Thermo Nicolet Corp.) equipped with a HgCdTe (MCT) detector and averaged over 512 scans with a spectral resolution of 32 cm⁻¹. As illustrated in Figure 1b, the polarization at the sample focus was set perpendicular to the slot axis as required for excitation of slot antenna resonances.

Near-field measurements were performed by scattering-type scanning near-field optical microscopy (s-SNOM) based on an atomic force microscope (AFM, Innova, Bruker Corp.) in noncontact imaging mode (see Figure 1) as described previously.^{16,39} For that purpose, mid-IR light was generated by difference frequency generation (DFG) in a GaSe crystal of the signal and idler beam from a fan-poled LiNbO₃-based optical parametric oscillator (OPO, Chameleon, Coherent Inc.) pumped by a Ti:sapphire oscillator (Mira-HP, Coherent, Inc.). The IR radiation (~280 μW, full width at half-maximum bandwidth of 85 cm⁻¹, pulse duration of 220 fs, and repetition rate of 80 MHz), polarized normal to the slot orientation, is focused to a nearly diffraction-limited spot at the tip-sample region with side illumination, using a 25.4 mm working distance 90° off axis parabolic (OAP) reflector. The tip-scattered antenna near-field is collected by the same parabolic mirror in a backscattering geometry and filtered by a vertical polarizer before being directed to a MCT detector, where it is detected interferometrically. Demodulation of the signal at the second or higher harmonic of the tip-dither frequency Ω_{AFM} using a lock-in amplifier suppresses the far-field background signal.³⁹ s-SNOM imaging provides a two-dimensional map of the *z* component of the electric near-field *E_z*, assisted by the preferential scattering of the tip-parallel field component. Homodyne interference and reference phase are adjusted such that the *E_z* near-field signal is symmetric with respect to

the substrate nonresonant background, as is adequate for imaging resonant structures with a simple 90° phase behavior.

For a full three-dimensional field simulation of the slot antenna, two commercial finite-element analysis software packages were employed independently and for comparison (COMSOL Multiphysics and ANSYS HFSS). The simulated geometry is a stack consisting of a substrate (KBr ε = 2.36, or Si ε = 11.7), a 50 nm Au layer, and air at the top. A surrounding perfectly matched layer (PML) is added to prevent boundary reflections. The plane wave is simulated to be incident under variable angles with respect to the surface normal from the top air layer, and polarized normal to the slot orientation. The dielectric function of Au is taken from recent broadband spectroscopic ellipsometry measurements of a thermally evaporated sample.³⁸ Transmission spectra are obtained by calculating the transmission for each frequency. The spatial near-field distribution is calculated 30 nm above the sample surface.

In order to understand the resonant behavior and mode structure of a single slot antenna, we perform far-field transmission spectroscopy over a wide spectral range. Figure 2 shows the measured transmission spectrum of a *L* = 2.4 μm

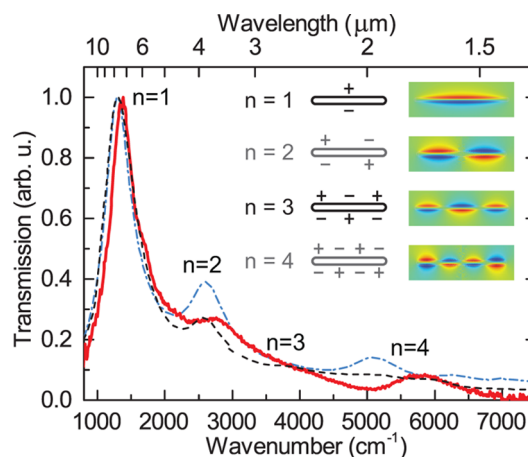


Figure 2. Resonant modes of a slot antenna. Experimental far-field transmission spectrum (solid red) for *L* = 2.4 μm slot compared to simulated spectrum (black dashed) and complementary rod antenna (blue dashed) with corresponding mode assignment. The four peak positions of the experimental spectrum are 1370, 2750, 4080, and 5790 cm⁻¹. Inset: Illustration of spatial near-field *E_z* distribution for different slot antenna modes or *B_z* for rod antenna, with odd (bright) and even (dark) modes.

slot on KBr (solid red line). It exhibits a pronounced fundamental dipole resonance at 1370 cm⁻¹, with a sequence of higher order modes. For comparison, we show the numerical simulation of an equal length slot (black dashed) with a 20° angle of incidence with respect to the surface normal with polarization perpendicular to the slot direction. We also show the calculated spectrum of the complementary rod antenna (blue dashed). The simulated spectra are convoluted with a Lorentzian function of 30 cm⁻¹ line width to account for inhomogeneity in antenna structure and excitation focus. The difference in line width may be due to losses from surface roughness and different effective gold dielectric constant between experiment and simulation.³⁸

From the calculation, four modes can be assigned within the spectral range, labeled *n* = 1–4. These modes correspond to the

first four lowest-order magnetic resonant eigenmodes of the slot antenna. The inset shows the corresponding schematic spatial near-field E_z distributions. The $n = 2$ and 4 modes are dark modes and are normally forbidden for plane wave excitation at normal incidence. However, the excitation of these modes becomes allowed because of tilted incidence from the Schwarzschild-type objective. The relative intensity of the four resonance peaks depends on the details of the incident field distribution. In agreement with theory, the peak of the $n = 3$ mode appears embedded in the shoulder of the $n = 2$ resonance. The small difference in peak position between experiment and theory can most likely be attributed to small differences in geometry and dielectric function between the fabricated and simulated structures.

Figure 3 shows the evolution of the measured spectral behavior for slots of varying length from $L = 0.5$ to $2.4 \mu\text{m}$. The

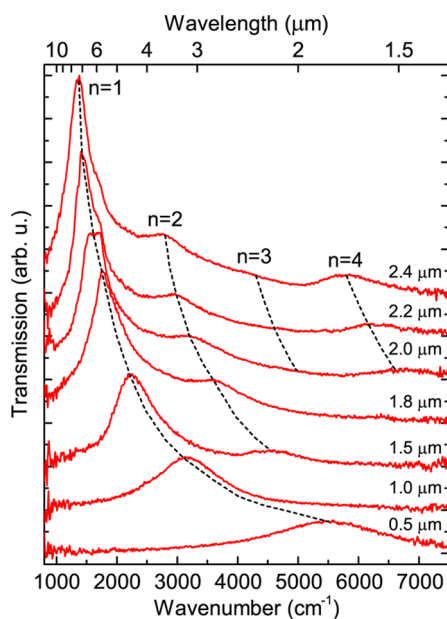


Figure 3. Transmission spectra of individual slot antennas on KBr substrate. For each length, the main peak corresponds to the fundamental dipolar magnetic resonance of the slot antenna $n = 1$, with higher order modes $n = 2, 3$, and 4 present depending on length.

peak transmission in each spectrum is normalized with respect to the peak transmission of the $L = 2.4 \mu\text{m}$ spectrum. For each slot length, the dominant peak corresponds to the fundamental dipolar resonance ($n = 1$) and shifts to lower frequency with increasing slot length. Higher order resonant modes shift correspondingly and decrease in amplitude with decreasing slot length.

The relation of slot length to the resonant wavelength can be derived from the transmission spectra. The antenna resonance can be explained by a Fabry-Pérot model when propagating plasmon modes form standing waves,^{40–44} given by

$$L + \frac{\delta}{2\pi}\lambda_p = n \times (\lambda_p/2) \quad (1)$$

with antenna length L , plasmon wavelength of a propagating plasmon mode λ_p , phase shift δ due to reflection of plasmon wave at the antenna end, and resonance mode number n .

For an ideal slot antenna cut from a film suspended in free space, dipole resonance occurs when the length is approximately $\lambda/2$.⁴⁵ With the slot patterned on a dielectric half-space,

together with the finite conductivity of the metal at optical frequencies and the low aspect ratios compared to the ideal narrow slot antenna, the resonant wavelength is red-shifted.

Figure 4 shows the dependence of resonant wavelengths determined from the peak positions as a function of slot length

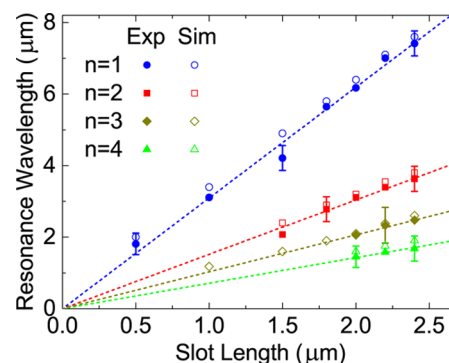


Figure 4. Resonant wavelength scaling of slot antennas. Resonance wavelengths from experiment (solid symbol) for $n = 1$ (blue circle), $n = 2$ (red square), $n = 3$ (dark yellow diamond), and $n = 4$ (green triangle) scale linearly with slot length, and can be described by $L = n \times \lambda_{\text{eff}}/2$ with a common value of $\lambda_{\text{eff}} = (0.64 \pm 0.05)\lambda$ for $n = 1-4$, in agreement with simulation (open symbol).

for the four modes. The length scaling can effectively be described by

$$L + \Delta L = n \times \lambda_{\text{eff}}/2 \quad (2)$$

for $n = 1-4$, with an apparent length increase of $\Delta L = \delta/(2\pi) \times \lambda_p$ due to the phase shift at the antenna end.⁴⁶ The apparent length increase ΔL is approximately the width of the antenna^{40–42,44,47} and is negligible because of the large aspect ratio >10 for the slots in our experiment. For $\Delta L = 0$, we obtain an effective wavelength $\lambda_{\text{eff}} = (0.64 \pm 0.05)\lambda$ from the simultaneous fit to all four modes, as shown in Figure 4.

Based on the resonant characteristics determined from far-field spectroscopy, we measure the corresponding near-field spatial distribution for selected antenna modes. Figure 5 shows s-SNOM images (b,e) of the relative E_z electric field component for two different slot lengths $L = 2.2$ and $1.6 \mu\text{m}$ corresponding to the $n = 1$ and 3 modes for an excitation

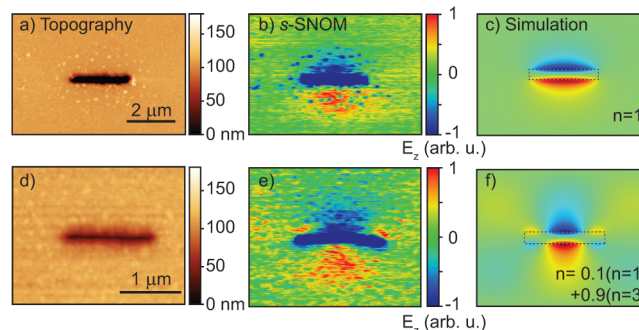


Figure 5. Optical near-field E_z of slot antenna at different resonances. Topography (a), s-SNOM (b), and simulation (c) of the fundamental $n = 1$ resonance of $L = 2.2 \mu\text{m}$ slot antenna on Si substrate. Corresponding measurements (d, e) and simulation (f) of the $L = 1.6 \mu\text{m}$ slot antenna on Si substrate. The optical near-field (e) shows a superposition of $n = 1$ and 3 resonance modes measured at a frequency slightly red detuned from the exact resonance of the $n = 3$ mode.

wavelength of $\lambda = 8.7$ and $5.7 \mu\text{m}$, respectively. The color scale reflects the regions of E_z pointing in and out of the sample plane, corresponding to an associated π phase change. Figure Sc,f shows the result of field simulations for the given geometries and excitation wavelengths. This confirms that the experimentally observed field pattern corresponds to the fundamental $n = 1$ mode (b,c), and the $n = 3$ mode (e,f) with a slight admixture of the fundamental mode responsible for the stronger than expected center lobes.

For the fundamental $n = 1$ mode, as shown in Figure Sb,c, the field distribution in three dimensions is circulating around the center axis of the slot and decreasing in intensity in the radial direction and toward the end of the slot. This type of electric field distribution of the $n = 1$ mode thus corresponds to the electric field of a virtual oscillating magnetic dipole oriented along the slot. Correspondingly, the higher order modes can be viewed as a superposition of multiple magnetic dipoles aligned in series.

The effective wavelength $\lambda_{\text{eff}} = (0.64 \pm 0.05)\lambda$ obtained from experimental spectra for the slot on a KBr substrate agrees with the corresponding numerical simulation result of $\lambda_{\text{eff}} = 0.63\lambda$. The value can be understood considering the substrate material with permittivity ϵ and the geometry of the slot with width W and length L from the relationship derived for the RF spectral region:⁴³

$$\lambda_{\text{eff}} = 0.97 \times \frac{1}{\sqrt{\epsilon_{\text{eff}}(1 + W/L)}} \times \lambda \quad (3)$$

where $\epsilon_{\text{eff}} = (1 + \epsilon)/2$ is the mean permittivity of substrate ϵ and air. The factor 0.97 is twice the exact scaling value associated with the fundamental dipole resonance $L = 0.485\lambda$.⁴⁸ In this expression, the inhomogeneous environment of air and substrate is approximated as an effective homogeneous medium.⁴⁹ For a slot antenna on a KBr substrate ($\epsilon = 2.36$), eq 3 then results in $\lambda_{\text{eff}} = 0.67\lambda$, consistent with our experiment and numerical simulation. As another example, for the case of an IR slot antenna on a Si substrate ($\epsilon = 11.7$), the predicted $\lambda_{\text{eff}} = 0.35\lambda$ also agrees with the result of a full electromagnetic simulation value of $\lambda_{\text{eff}} = (0.33 \pm 0.05)\lambda$.

Equation 3, although derived for RF, is also applicable in the IR, with the effective medium chosen as the mean permittivity of air and substrate ϵ at the corresponding IR frequency. The reason for its validity within the Drude regime can be understood from the planar surface plasmon dispersion relation,⁴⁶ $k^2 = (\omega^2/c^2)[\epsilon_m \epsilon_s / (\epsilon_m + \epsilon_s)]$, with dielectric function of metal ϵ_m and its surrounding ϵ_s . The planar surface plasmon dispersion relation is approximately linear and follows the light line of $k = \omega/c\sqrt{\epsilon_s}$ with a difference in k -vector $< 1\%$ for wavelength $\gtrsim 2 \mu\text{m}$ at a gold and KBr interface.^{50–52} The propagation loss is also small in the IR with negligible effect on the resonance peak position. Only when the wavelength scaling becomes nonlinear, eq 3 begins to fail and Babinet's principle starts to break down.

To verify Babinet's principle, we compare the slot antenna length scaling with its complementary rod antenna. The complementary Au rod antenna on KBr has been previously measured with $\lambda_{\text{eff}} = (0.68 \pm 0.06)\lambda$,⁴⁹ which agrees well with our measured result $\lambda_{\text{eff}} = (0.64 \pm 0.05)\lambda$ for the slot antenna. For a similar rod antenna on a Si substrate the effective wavelength was measured to be $\lambda_{\text{eff}} = (0.32 \pm 0.05)\lambda$,^{53,54} consistent with that of slot antenna on Si with $\lambda_{\text{eff}} = 0.35\lambda$ from eq 3.

Beyond far-field spectra our near-field imaging on the slot antenna resolved the $n = 1$ and 3 modes. Through simulation, the electric near-field and its spatial distribution of the slot E_2 is found to correspond to the magnetic distribution B_1 of the rod and is related through the duality relation $B_1 = -E_2/c$. This result quantitatively verifies that the magnetic field profile of a rod antenna can be determined by measuring the electric field distribution of a slot antenna. For example, for an incident field strength $E_0 \sim 10^6 \text{ V/m}$, we achieve a maximum electric field $E_2 \sim 2 \times 10^7 \text{ V/m}$ at the center of slot at the fundamental resonance, corresponding to a maximum magnetic field $B_1 \sim 0.06 \text{ T}$ for the complementary rod resonance.

In summary, the combination of far-field spectroscopy with near-field imaging quantifies the validity of Babinet's principle for Drude metals and wavelength $\gtrsim 2 \mu\text{m}$. Using Babinet's principle, we demonstrate a general method of probing the optical magnetic field from the study of the electric field of a complementary structure. This method of measuring the magnetic near-field and the resonance scaling provides an improved way to characterize optical antennas and metamaterials and to understand the magnetic light-matter interaction at the nanoscale.

AUTHOR INFORMATION

Corresponding Author

*E-mail: markus.raschke@colorado.edu.

Present Address

[§]Department of Chemistry, University of Toronto, Canada (X.G.X.).

Notes

The authors declare no competing financial interest.

ACKNOWLEDGMENTS

The authors thank C. Rockstuhl for helpful discussions. Part of the work was supported by a partner proposal with the Environmental Molecular Sciences Laboratory (EMSL), a national scientific user facility from the DOE Office of Biological and Environmental Research at Pacific Northwest National Laboratory (PNNL). PNNL is operated by Battelle for the U.S. DOE under Contract DEAC06-76RL01830. The Advanced Light Source is supported by the Director, Office of Science, Office of Basic Energy Sciences, of the U.S. Department of Energy under Contract No. DE-AC02-05CH11231. Funding from the National Science Foundation (1204993 and NSF Grant CHE 1306398) is gratefully acknowledged.

REFERENCES

- (1) Pendry, J.; Holden, A.; Robbins, D.; Stewart, W. Magnetism from conductors and enhanced nonlinear phenomena. *IEEE Trans. Microwave Theory Technol.* **1999**, *47*, 2075–2084.
- (2) Enkrich, C.; Wegener, M.; Linden, S.; Burger, S.; Zschiedrich, L.; Schmidt, F.; Zhou, J.; Koschny, T.; Soukoulis, C. Magnetic metamaterials at telecommunication and visible frequencies. *Phys. Rev. Lett.* **2005**, *95*, 203901.
- (3) Aouani, H.; Mahboub, O.; Bonod, N.; Devaux, E.; Popov, E.; Rigneault, H.; Ebbesen, T. W.; Wenger, J. Bright unidirectional fluorescence emission of molecules in a nanoaperture with plasmonic corrugations. *Nano Lett.* **2011**, *11*, 637–644.
- (4) Karaveli, S.; Zia, R. Spectral tuning by selective enhancement of electric and magnetic dipole emission. *Phys. Rev. Lett.* **2011**, *106*, 193004.

- (5) Kihm, H. W.; Koo, S. M.; Kim, Q. H.; Bao, K.; Kihm, J. E.; Bak, W. S.; Eah, S. H.; Lienau, C.; Kim, H.; Nordlander, P.; Halas, N. J.; Park, N. K.; Kim, D.-S. Bethe-hole polarization analyser for the magnetic vector of light. *Nat. Commun.* **2011**, *2*, 451.
- (6) Jitrik, O. Transition probabilities for hydrogen-like atoms. *J. Phys. Chem. Ref. Data* **2004**, *33*, 1059–1070.
- (7) Giessen, H.; Vogelgesang, R. Physics. Glimpsing the weak magnetic field of light. *Science (New York, N.Y.)* **2009**, *326*, 529–530.
- (8) Cowan, R. D. *The Theory of Atomic Structure and Spectra*; University of California Press: California, U.S.A., 1981.
- (9) Grosjean, T.; Mivelle, M.; Baida, F. I.; Burr, G. W.; Fischer, U. C. Diabolo nanoantenna for enhancing and confining the magnetic optical field. *Nano Lett.* **2011**, *11*, 1009–1013.
- (10) Koo, S.; Kumar, M. S.; Shin, J.; Kim, D.; Park, N. Extraordinary magnetic field enhancement with metallic nanowire: role of surface impedance in babinet's principle for sub-skin-depth regime. *Phys. Rev. Lett.* **2009**, *103*, 263901.
- (11) Feng, T.; Zhou, Y.; Liu, D.; Li, J. Controlling magnetic dipole transition with magnetic plasmonic structures. *Opt. Lett.* **2011**, *36*, 2369–2371.
- (12) Klein, M. W.; Enkrich, C.; Wegener, M.; Linden, S. Second-harmonic generation from magnetic metamaterials. *Science (New York, N.Y.)* **2006**, *313*, 502–504.
- (13) Kabashin, V.; Evans, P.; Pastkovsky, S.; Hendren, W.; Wurtz, G.; Atkinson, R.; Pollard, R.; Podolskiy, V. a.; Zayats, V. Plasmonic nanorod metamaterials for biosensing. *Nat. Mater.* **2009**, *8*, 867–871.
- (14) Hein, S. M.; Giessen, H. Tailoring magnetic dipole emission with plasmonic split-ring resonators. *Phys. Rev. Lett.* **2013**, *111*, 026803.
- (15) Buresi, M.; van Oosten, D.; Kampfrath, T.; Schoenmaker, H.; Heideman, R.; Leinse, a.; Kuipers, L. Probing the magnetic field of light at optical frequencies. *Science (New York, N.Y.)* **2009**, *326*, 550–553.
- (16) Olmon, R. L.; Rang, M.; Krenz, P. M.; Lail, B. A.; Saraf, L. V.; Boreman, G. D.; Raschke, M. B. Determination of electric-field, magnetic-field, and electric-current distributions of infrared optical antennas: a near-field optical vector network analyzer. *Phys. Rev. Lett.* **2010**, *105*, 167403.
- (17) Seo, M. A.; Adam, A. J. L.; Kang, J. H.; Lee, J. W.; Jeoung, S. C.; Park, Q. H.; Planken, P. C. M.; Kim, D. S. Fourier-transform terahertz near-field imaging of one-dimensional slit arrays: mapping of electric-field-, magnetic-field-, and Poynting vectors. *Opt. Express* **2007**, *15*, 11781–11789.
- (18) Schnell, M.; Garcia-Etxarri, a.; Alkorta, J.; Aizpurua, J.; Hillenbrand, R. Phase-resolved mapping of the near-field vector and polarization state in nanoscale antenna gaps. *Nano Lett.* **2010**, *10*, 3524–3528.
- (19) Grosjean, T.; Ibrahim, I. A.; Suarez, M. A.; Burr, G. W.; Mivelle, M.; Charraut, D. Full vectorial imaging of electromagnetic light at subwavelength scale. *Opt. Express* **2010**, *18*, 5809–5824.
- (20) Kihm, H. W.; Kim, J.; Koo, S.; Ahn, J.; Ahn, K.; Lee, K.; Park, N.; Kim, D.-S. Optical magnetic field mapping using a subwavelength aperture. *Opt. Express* **2013**, *21*, 5625–5633.
- (21) Denkova, D.; Verellen, N.; Silhanek, A. V.; Valev, V. K.; Van Dorpe, P.; Moshchalkov, V. V. Mapping magnetic near-field distributions of plasmonic nanoantennas. *ACS Nano* **2013**, *7*, 3168–3176.
- (22) le Feber, B.; Rotenberg, N.; Beggs, D. M.; Kuipers, L. Simultaneous measurement of nanoscale electric and magnetic optical fields. *Nat. Photonics* **2014**, *8*, 43–46.
- (23) García de Abajo, F. J. Colloquium: Light scattering by particle and hole arrays. *Rev. Mod. Phys.* **2007**, *79*, 1267–1290.
- (24) García-Vidal, F. J.; Martín-Moreno, L.; Ebbesen, T. W.; Kuipers, L. Light passing through subwavelength apertures. *Rev. Mod. Phys.* **2010**, *82*, 729–787.
- (25) Degiron, a.; Lezec, H.; Yamamoto, N.; Ebbesen, T. Optical transmission properties of a single subwavelength aperture in a real metal. *Opt. Commun.* **2004**, *239*, 61–66.
- (26) García-Vidal, F.; Moreno, E.; Porto, J.; Martín-Moreno, L. Transmission of light through a single rectangular hole. *Phys. Rev. Lett.* **2005**, *95*, 103901.
- (27) Zhang, J.; Zhang, W.; Zhu, X.; Yang, J.; Xu, J.; Yu, D. Resonant slot nanoantennas for surface plasmon radiation in optical frequency range. *Appl. Phys. Lett.* **2012**, *100*, 241115.
- (28) Ögüt, B.; Vogelgesang, R.; Sigle, W.; Talebi, N.; Koch, C. T.; van Aken, P. a. Hybridized metal slit eigenmodes as an illustration of Babinet's principle. *ACS Nano* **2011**, *5*, 6701–6706.
- (29) Hentschel, M.; Weiss, T.; Bagheri, S.; Giessen, H. Babinet to the half: coupling of solid and inverse plasmonic structures. *Nano Lett.* **2013**, *13*, 4428–4433.
- (30) Ishimaru, A. *Electromagnetic Wave Propagation, Radiation, and Scattering*; Prentice-Hall, Inc.: Englewood Cliffs, NJ, 1991.
- (31) Stutzman, W. L.; Thiele, G. A. *Antenna Theory and Design*, 2nd ed.; Wiley: New York, 1997.
- (32) Balanis, C. A. *Antenna Theory: Analysis and Design*; John Wiley & Sons, Inc.: New York, 1997; Vol. 46, p 960.
- (33) Booker, H. Slot aerials and their relation to complementary wire aerials (Babinet's principle). *J. Inst. Electr. Eng., Part 3* **1946**, *93*, 620–626.
- (34) Falcone, F.; Lopetegi, T.; Laso, M.; Baena, J.; Bonache, J.; Beruete, M.; Marqués, R.; Martín, F.; Sorolla, M. Babinet principle applied to the design of metasurfaces and metamaterials. *Phys. Rev. Lett.* **2004**, *93*, 197401.
- (35) Bitzer, A.; Ortner, A.; Merbold, H.; Feurer, T.; Walther, M. Terahertz near-field microscopy of complementary planar metamaterials: Babinet's principle. *Opt. Express* **2011**, *19*, 2537–2545.
- (36) Zentgraf, T.; Meyrath, T.; Seidel, a.; Kaiser, S.; Giessen, H.; Rockstuhl, C.; Lederer, F. Babinet's principle for optical frequency metamaterials and nanoantennas. *Phys. Rev. B* **2007**, *76*, 033407.
- (37) Rockstuhl, C.; Zentgraf, T.; Meyrath, T. P.; Giessen, H.; Lederer, F. Resonances in complementary metamaterials and nanoapertures. *Opt. Express* **2008**, *16*, 2080–2090.
- (38) Olmon, R. L.; Slovick, B.; Johnson, T. W.; Shelton, D.; Oh, S.-h.; Boreman, G. D.; Raschke, M. B. Optical dielectric function of gold. *Phys. Rev. B* **2012**, *86*, 235147.
- (39) Olmon, R. L.; Krenz, P. M.; Jones, A. C.; Boreman, G. D.; Raschke, M. B. Near-field imaging of optical antenna modes in the mid-infrared. *Opt. Express* **2008**, *16*, 20295–20305.
- (40) Novotny, L. Effective wavelength scaling for optical antennas. *Phys. Rev. Lett.* **2007**, *98*, 266802.
- (41) Hasan, S. B.; Filter, R.; Ahmed, A.; Vogelgesang, R.; Gordon, R.; Rockstuhl, C.; Lederer, F. Relating localized nanoparticle resonances to an associated antenna problem. *Phys. Rev. B* **2011**, *84*, 195405.
- (42) Søndergaard, T.; Beermann, J.; Boltasseva, A.; Bozhevolnyi, S. Slow-plasmon resonant-nanostrip antennas: Analysis and demonstration. *Phys. Rev. B* **2008**, *77*, 115420.
- (43) Dorfmueller, J.; Vogelgesang, R.; Khunsin, W.; Rockstuhl, C.; Etrich, C.; Kern, K. Plasmonic nanowire antennas: experiment, simulation, and theory. *Nano Lett.* **2010**, *10*, 3596–3603.
- (44) Bryant, G. W.; García de Abajo, F. J.; Aizpurua, J. Mapping the plasmon resonances of metallic nanoantennas. *Nano Lett.* **2008**, *8*, 631–636.
- (45) Kominami, M.; Pozar, D.; Schaubert, D. Dipole and slot elements and arrays on semi-infinite substrates. *IEEE Trans. Antennas Propag.* **1985**, *33*, 600–607.
- (46) Dorfmueller, J.; Vogelgesang, R.; Weitz, R. T.; Rockstuhl, C.; Etrich, C.; Pertsch, T.; Lederer, F.; Kern, K. Fabry-Pérot resonances in one-dimensional plasmonic nanostructures. *Nano Lett.* **2009**, *9*, 2372–2377.
- (47) Gordon, R. Reflection of cylindrical surface waves. *Opt. Express* **2009**, *17*, 18621–18629.
- (48) Olmon, R. L.; Raschke, M. B. Antenna-load interactions at optical frequencies: impedance matching to quantum systems. *Nanotechnology* **2012**, *23*, 444001.
- (49) Neubrech, F.; Kolb, T.; Lovrincic, R.; Fahsold, G.; Pucci, a.; Aizpurua, J.; Cornelius, T. W.; Toimil-Molares, M. E.; Neumann, R.

Karim, S. Resonances of individual metal nanowires in the infrared. *Appl. Phys. Lett.* **2006**, *89*, 253104.

(50) Schider, G.; Krenn, J.; Hohenau, a.; Ditlbacher, H.; Leitner, a.; Aussenegg, F.; Schaich, W.; Puscasu, I.; Monacelli, B.; Boreman, G. Plasmon dispersion relation of Au and Ag nanowires. *Phys. Rev. B* **2003**, *68*, 155427.

(51) Wang, K.; Mittleman, D. Dispersion of surface plasmon polaritons on metal wires in the terahertz frequency range. *Phys. Rev. Lett.* **2006**, *96*, 157401.

(52) Chen, Y.; Song, Z.; Li, Y.; Hu, M.; Xing, Q.; Zhang, Z.; Chai, L.; Wang, C.-Y. Effective surface plasmon polaritons on the metal wire with arrays of subwavelength grooves. *Opt. Express* **2006**, *14*, 13021.

(53) Fumeaux, C.; Gritz, M. A.; Codreanu, I.; Schaich, W. L.; González, F. J.; Boreman, G. D. Measurement of the resonant lengths of infrared dipole antennas. *Infrared Phys. Technol.* **2000**, *41*, 271–281.

(54) Crozier, K. B.; Sundaramurthy, a.; Kino, G. S.; Quate, C. F. Optical antennas: Resonators for local field enhancement. *J. Appl. Phys.* (Melville, NY, U. S.) **2003**, *94*, 4632.

■ NOTE ADDED AFTER ASAP PUBLICATION

This paper originally posted ASAP on August 18, 2014. A correction was made in the second paragraph in the sentence citing references 15, 20–22. The corrected version was reposted on September 3, 2014.